BNL-63249
(REV. 08/96)
Informal Report

CONF-9605189--7-Rev.08/96

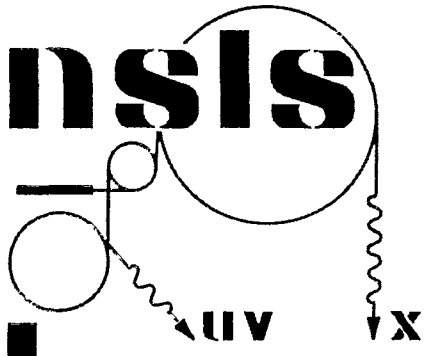

CO_2 LASER TECHNOLOGY FOR ADVANCED PARTICLE ACCELERATORS

I.V. Pogorelsky

June 1996

NATIONAL SYNCHROTRON LIGHT SOURCE

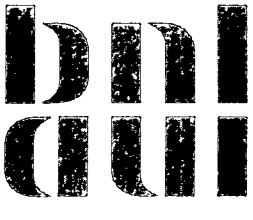

BROOKHAVEN NATIONAL LABORATORY
ASSOCIATED UNIVERSITIES, INC.
Under Contract No. DE-AC02-76CH00016 with the
UNITED STATES DEPARTMENT OF ENERGY

DISCLAIMER

BNL-63249
(REV. 08/96)
Informal Report

CO_2 LASER TECHNOLOGY FOR ADVANCED PARTICLE ACCELERATORS

I.V. Pogorelsky

June 1996

Based on talk presented at the Meeting of American Physical Society, May 2-8, 1996, Indianapolis, IN

CO_2 LASER TECHNOLOGY FOR ADVANCED PARTICLE ACCELERATORS

I.V. Pogorelsky
Accelerator Test Facility, Brookhaven National Laboratory, 725C, Upton, NY 11973

Abstract

Short-pulse, high-power CO_2 lasers open new prospects for development of ultra-high gradient laser-driven electron accelerators. The advantages of λ=10 μm CO_2 laser radiation over the more widely exploited solid state lasers with $\lambda\approx1$ μm are based on a λ^2-proportional ponderomotive potential, λ-proportional phase slippage distance, and λ-proportional scaling of the laser accelerator structures. We show how a picosecond terawatt CO_2 laser that is under construction at the Brookhaven Accelerator Test Facility may benefit the ATF's experimental program of testing far-field, near-field, and plasma accelerator schemes.

I. Introduction

Lasers are the sources of the most intense electromagnetic radiation and strongest electric and magnetic fields readily available for laboratory research. For example, focusing of a terawatt laser beam into a 10 μm spot results in intensity of 10^{18} W/cm^2 and, associated with it, an electric field of 30 GV/cm that exceeds by five orders of magnitude accelerating fields attainable in conventional particle accelerators. Such capability stimulated a new high-energy physics discipline to emerge: laser-driven high-gradient particle accelerators. Search for novel and more economical mechanisms of particle acceleration has acquired special importance after the demise of the SSC project. Experimental activity in this field has been vitalized by recent development of, so called, T^3 (table-top terawatt) lasers based on mode-locked picosecond pulse generation and frequency-chirped amplification in laser-active glasses or crystals operating at wavelengths near $\lambda\approx1$ μm.

Downside of the progress in picosecond solid state laser technology was the diverted attention from the high-power CO_2 lasers that have been traditionally attractive for strong-field physics applications due to the feasibility of fairly economical large-volume devices with high-energy output and high repetition rates.

Indeed, there are two major problems associated with relatively long-wavelength ($\lambda\approx10$ μ m) CO_2 lasers when trying to attain ultra-high electromagnetic fluxes. First is a wavelength-proportional diffraction divergence that results in larger spot sizes and shorter Rayleigh distances at the laser beam focusing. Second, because of the relatively narrow rotational structure typical for molecular gas spectra, picosecond pulse formation and amplification have not been as successfully obtained with CO_2 lasers as with solid state lasers, which have wide crystal-host broadening of the individual ion spectral lines. Fortunately, these complications are not fatal and may be overcome by mobilizing high-pressure gas laser technology and laser beam channeling methods, as will be discussed below.

Provided the picosecond terawatt CO_2 (psTW-CO_2) lasers become a reality, their attractive features for strong-field applications, such as laser-driven particle acceleration, come into play. There are a number of considerations that call for wider application of long-

wavelength psTW-CO_2 lasers as advanced particle accelerator drivers. Maybe the most fundamental advantage of slow-oscillating fields for particle acceleration stems from the fact that the energy of oscillatory motion acquired by the electron from an electromagnetic wave is quadratically proportional to the wavelength. Hence, any process, where the field-induced electron oscillation is paramount, is dramatically enhanced. The examples of such processes are: relativistic self-focusing, avalanche and tunneling ionization, and plasma wave excitation, which are especially relevant for electron acceleration in a plasma.

Conventional subnanosecond, multigigawatt CO_2 laser beams, intensity-modulated with the period of a plasma wave, have been used successfully in laser beat wave accelerator (LBWA) experiments[1,2], where up to 30 MeV electron acceleration over a 1 cm interaction distance has been demonstrated. The efficiency of plasma acceleration schemes, that, in addition to LBWA, include laser wakefield accelerator (LWFA)[3] and their modifications, is greatly enhanced by laser power increase and pulse shortening. However, the major limitation to further scaling up of the plasma-based laser accelerators is the short focal region where high laser intensity may be maintained. For typical conditions of plasma acceleration experiments, this distance is limited to a few millimeters. A possible way to increase the acceleration distance is channeling of laser beams. Plasma channels produced under gas ionization by axicon-focused laser beams may be used as waveguides for laser-driven plasma accelerators[4,5]. Being a good ionizer, the CO_2 laser is a good choice for plasma channel formation as well.

Among known plasma-based laser acceleration techniques, self-modulated (SM) LWFA[6] looks presently the most promising. This method requires a so called "relativistically strong" laser beam that satisfies conditions for relativistic self-focusing in plasma. Simulations demonstrate a possibility to accelerate electrons from 50 MeV to the 500 MeV absolute energy over a 4 cm distance using properly shaped 5 TW CO_2 laser pulses propagating inside a plasma channel[7].

CO_2 lasers look attractive for not just acceleration in plasma. In general, particle acceleration by a fast-oscillating electromagnetic field becomes possible when a relativistic particle moves in synchronism with the phase of the driving field. The long wavelength of a CO_2 laser helps to meet this requirement. This feature, is of particular importance for far-field acceleration schemes, examples of which are the Inverse Cherenkov Accelerator (ICA)[8,9] and Inverse Free Electron Laser (IFEL) accelerator[10,11].

Proposed near-field accelerator schemes (Grating Linac[12] and Resonant Accelerator[13]) are based on the accelerating action of evanescent fields developed near the periodically shaped surfaces under laser irradiation. Since the spatial scale of such structures is comparable with the laser wavelength, these schemes look practical when a CO_2 or longer-wavelength laser is used as the accelerator driver.

The approach to utilize the long-wavelength laser radiation for particle acceleration study is pursued at the Brookhaven Accelerator Test Facility (ATF) where the first psTW-CO_2 laser is under construction to demonstrate high-gradient electron acceleration using far-field, near-field, and plasma acceleration schemes.

II. Emerging Picosecond Terawatt CO_2 Laser Technology

II.1 Bandwidth Restrictions

In solid state lasers, radiation transitions in outer electron shells of active ions exhibit broadening to 5-50 THz due to the perturbation action of a host matrix. Such a broad gain spectrum makes possible the generation and amplification of picosecond and even femtosecond laser pulses. On the contrary, it has been realized that to build a picosecond CO_2 laser is a problem because the spectral gain in the gas discharge is periodically modulated by a molecular

rotational structure. Due to the discrete spectrum, and for other technical reasons, mode-locking techniques do not work for CO_2 lasers as well as for solid state lasers. Such a modulated spectrum impedes also amplification of picosecond pulses.

When photons with $\lambda \approx 10$ μm propagate in the CO_2 laser medium, two characteristic time constants should be taken into consideration. The first is the time interval, δt, reciprocal of the spectral period of the CO_2 rotational structure, which is 18 ps for the P-branch of the 10-μm band. Second characteristic parameter is a collisionally induced dipole dephasing time, T_2, related to the pressure-broadened rotational line width, $\delta\nu$, by the ratio $\pi T_2 = \delta\nu^{-1}$. For 1-atm CO_2-laser, $T_2 \approx 100$ ps.

If the input laser pulse is shorter than 18 ps, its spectrum covers several discrete transition lines. The electric field of such an input pulse excites a polarization in CO_2 molecules, which are in various rotational states. Since molecules in different states are characterized by different frequencies, these polarization components eventually become dephased. As a result, the spectral and time structure of the induced radiation will not remain equal to those of the initial pulse. At a low, ~1 atm, gas pressure the discrete gain spectrum transforms the spectrum of the input pulse from continuous to discrete, and its inverse Fourier transform corresponds to a pulse train with a δt period. At higher pressure, the broadening effect smoothes the discrete gain spectrum. As a result the pulse splitting is reduced and ultimately disappears at the amplifier pressure of 15 atm.

An alternative to achieve gain smoothing is a reduction of the spectrum modulation period using a multi-isotope gas mixture. Replacement of one of the oxygen nuclei by that of a different isotope destroys the symmetry of the CO_2 molecule. That means that twice as many V-R transitions are allowed and the gain spectrum becomes twice as dense as with a regular CO_2 molecule. If we consider a mixture of $^{12}C^{16}O_2$:$^{12}C^{16}O^{18}O$:$^{12}C^{18}O_2$ = 1:2:1, then, due to isotopic shifts, the combined spectrum will have in overlap regions an approximately 4-times denser rotational line structure than with a regular CO_2 molecule. Computer modeling[14] shows that the reduction in spectral line interval, together with pressure broadening, results in considerably less short-pulse distortion during amplification. The technical advantage of this approach is related to the greater ease of establishing a large-aperture stable discharge at 4-5 atm in comparison to 10-15 atm.

At the total bandwidth of the 10P CO_2 branch $\Delta\nu \approx 1$ THz, the fundamental limit for the laser pulse duration, as defined by the ratio $\Delta\nu \times \tau \approx 0.5$, is $\tau \approx 0.5$ ps. As short as 0.6 ps CO_2 laser pulses have been demonstrated from a high-pressure regenerative amplifier[15].

II.2 Generation of Picosecond CO_2 Laser Pulses

There are two methods to produce picosecond and sub-picosecond CO_2-laser pulses. Both of them require a short-wavelength, short-pulse laser. By frequency mixing in a nonlinear crystal the difference frequency at 10 μm may be generated in a parametric oscillator. At the ATF we use another method, semiconductor switching, to generate picosecond CO_2 laser pulses of a variable duration.

The semiconductor optical switching method is based on the modulation of the reflective and transmissive properties of a semiconductor by optically controlling the free-carrier charge density. A short-wavelength picosecond laser pulse with a photon energy above the band gap of the semiconductor creates a highly reflective electron-hole plasma in the surface layer of a semiconductor, such as germanium, which is normally transparent to 10-μm radiation. The free-electron density, N_e, at the semiconductor surface is linearly proportional to the absorbed control pulse fluence E, such that

$$N_e = \alpha E / h\nu, \qquad (1)$$

where α is the absorption coefficient and $h\nu$ is the photon energy. For a Nd:YAG control laser, α^{-1}=1 μm, and, for a characteristic pulse fluence of E≈2 mJ/cm^2, the density of the excess free carriers, N_e, created in Ge exceeds the critical density of N_{cr}=1.6x10^{19}/cm^3 defined by

$$N_{cr}=\omega^2 m_0 n_0^2/4\pi e^2, \quad (2)$$

where ω is the radiation frequency, m_e- reduced free carrier mass, n_0 - refractive index at normal conditions. The refractive index drops due to free carriers according to the equation

$$n=n_0(1-N_e/N_{cr})^{1/2} \quad (3)$$

and turns imaginary at $N_e>N_{cr}$. At this moment, Ge slab switches from a window at λ=10 μm to a highly reflective mirror due to its "metallization" by a picosecond Nd:YAG control pulse.

After the termination of the control pulse, the main process governing the time evolution of the excess free carriers at the surface of the Ge slab, and hence the reflectivity, will be ambipolar diffusion having a characteristic time constant of 150 ps in Ge. To define the trailing edge of the pulse, shortening it to a few picoseconds, the complement to reflection switching, transmission switching, may be used for a second stage. An optically delayed control pulse cuts off the trailing edge of the transient pulse by initiating reflection and absorption. The resulting "sliced" transmitted pulse has a variable length defined by optical delay adjustment of the control radiation before the transmission switch. Optical diagram of the double-switch configuration used at the ATF is shown in Fig.1.

Instead of the transmission switch in a double semiconductor slicer configuration, the transient response of a thin etalon can be exploited[16]. The etalon tuned to minimum reflectivity serves as a differentiator transmitting radiation with a constant or slow-varying intensity but reflecting at intensity gradients shorter than the double optical thickness of the etalon. For instance, 100-μm thick Ge etalon placed after the reflection switch may serve for efficient differentiating of transient pulse with a steep leading front, producing ~ 3-ps high-contrast IR pulses.

Another way to eliminate the tail in the reflected pulse is to use a semiconductor material with previously introduced radiation damage to the lattice structure. For such materials, subpicosecond electron-hole recombination times have been measured[17]. Then, the second semiconductor optical switch is not needed, and the reflected CO_2 laser pulse is close to the control pulse duration.

II.3 Amplification of Picosecond CO_2 Laser Pulses

When estimating laser amplifier efficiency, the following two physical parameters play the major role: a small signal gain $g_0=\sigma N^*$, where σ - gain cross-section, and N^* - population inversion at the laser levels; and saturation fluence $E_s=h\nu/2\sigma$.

Parameters g_o and E_s regulate the energy amplification process described by Franz-Nodvik equation

$$E_{out} = E_s \ln\{1 + \exp(g_0 l)[\exp(E_{in}/E_s) - 1]\}. \quad (4)$$

The product of these parameters gives also an estimate of the energy potentially extractable from the amplifier in a single pass in a strongly saturated regime:

$$E_{max}= g_0 E_s l S, \quad (5)$$

where l and S are, correspondingly, the length and aperture of the amplifier.

The ratio E_{max}/τ characterizes the peak laser power from the amplifier. We know already that the pressure increase helps to reduce the pulse duration, τ. Now, we need to understand how E_{max} depends upon the pressure.

Due to pressure broadening of the gain spectrum, there is a linear proportionality of E_s to the pressure via the parameter σ. The small signal gain, g_0, is inversely proportional to σ. However, g_0 depends also upon N^* which is subject to the electric discharge conditions. The electron-molecule collision frequency and, hence, the pump rate both rise proportionally to the pressure. If the discharge is faster than collisional quenching of the inversion, then we may consider $N^* \sim P$ and g_o invariant with pressure. Ultimately, we come to the conclusion, that $E_{max} \sim P$.

Computer simulation[14] for a τ_0=3 ps pulse propagating in a 10-atm amplifier gives $E_s \approx$ 500 mJ/cm^2 and, at the typical g_0=4%/cm, the extractable specific energy is $E_{max}/lS \approx 20$ mJ/cm^3. Taking into account that the total discharge volume may exceed 10 *l*, the possibility of extraction of as high as 100 J of energy in a few picosecond pulse from a single, reasonably compact CO_2 laser amplifier looks realistic. However, the limiting factor to the high energy extraction may be the damage threshold of the output window, $E_{th} \approx 500$ mJ/cm^2.[15] For an optical window of a 10× 10 cm^2 size, the extractable energy is 30-50 J that corresponds to ~10 TW peak power at a 3-ps laser pulse duration.

The main physical characteristics for solid state and CO_2 laser amplifiers are compiled in Table 1. It is interesting that gain cross-section per ion or molecule is comparable for both. However, about ten times higher concentration of active ions in solid state than CO_2 molecules in a gas makes gain about ten times higher for solid state lasers. About ten times heavier quant makes the specific stored energy about hundred times higher. However, much bigger volume of gas amplifiers makes the total stored energy per CO_2 amplifier stage similar or higher than for a big-size slab solid state amplifier. Because of the ease of the heat removal by fast gas exchange in the CO_2 amplifier, it is potentially capable of high repetition rates that are difficult to attain with solid optical elements. This may be important for future advanced particle accelerators.

II.4 Terawatt CO_2 Laser Project at the BNL Accelerator Test Facility

The projected terawatt CO_2 laser system is, the upgrade version of the presently operational 10-GW ATF CO_2 laser[18]. As long as a number of basic principles and elements of the present ATF laser will be preserved after the upgrade, it would be relevant to give its brief overview.

The ATF CO_2 laser system includes: a hybrid TEA oscillator, picosecond semiconductor switch, and a UV-preionized multipass TE amplifier.

In the laser oscillator, a diffraction grating tunes the laser wavelength stepwise between the individual rotational lines in the gain spectrum of the CO_2 molecules, which are vibrationally excited in the electric discharge. In addition to the 1-atm discharge-cell, the oscillator also includes an auxiliary low-pressure discharge cell. The narrow spectral line of the low-pressure discharge selects the particular longitudinal eigenmode to build-up inside the laser cavity. Piezo-tuning of the cavity length matches a mode spectral position to the gain peak. The output single-mode laser pulse has a smooth envelope, free from the stochastic mode-beat spikes otherwise typical for free-running TEA CO_2 lasers.

The semiconductor double-stage switching method described in paragraph II.2 is used to slice a 100-ns oscillator pulse to the desired picosecond width. A 10-ps Nd:YAG laser, that serves as a photocathode driver for the ATF linac, also supplies a 1.06-μm pulse for slicing. Using the same initiator for the linac and for the CO_2 pulse slicing ensures the desired picosecond synchronization of the electron bunch and laser pulse at their interaction region.

To reach a power level needed for laser accelerator studies, the switched picosecond pulse is transmitted through the 8-pass CO_2 amplifier that features a 120-cm long, 3-atm, UV-preionized, transverse electrical discharge energized by a 150-kV pulse. The limited spectral

bandwidth of the amplifier defines ~100 ps minimum duration of the output laser pulse. Thus, at the amplifier output energy of 1 J, the available peak power is ~10 GW.

The design concept for the CO_2 laser upgrade presumes slicing and then amplification of a short (~3 ps) laser pulse. We also expand the amplifier cross-section, thus allowing a high energy extraction through the large-aperture output window. Both pulse shortening and energy increase should permit an increase of the peak power from several GW to several TW level. Fig.2 presents a principal optical diagram for the modified CO_2 laser system. The presently operational oscillator and semiconductor switch will supply a picosecond seed pulse into a regenerative preamplifier which will share a portion of the active discharge region in a large-aperture multi-isotope amplifier. After the regenerative amplifier, four or five additional passes, with the laser beam expanded to ~80 cm^2, will boost the output power to the 5 TW level in a ~3-ps pulse[19,20].

Essential for the amplifier design is the discharge mechanism to create a uniform gas excitation in a ~10 *l* volume under high pressure. A self-sustained glow discharge can exist only at $dP \leq 0.1$ cm.atm. Above this point, an additional external uniform ionization should be applied to prevent discharge from arcing. The simplest corona and UV-preionization methods work well up to $dP \approx 15$-20 cm.atm. Above that level, more intense and volume-penetrating x-ray and e-beam preionizers are used. High ionization efficiency of e-beams makes it possible even to reduce the discharge voltage two times below the self-glow level (so called, e-beam sustained discharge). It helps to maintain the discharge at the optimum normalized field strength, V/dP, resulting in high efficiency of the upper laser level excitation. However, a high probability of e-beam window failure (usually thin metal foils), especially at a high pressure, makes e-guns inconvenient for this application.

X-ray preionization, while somewhat more complex than the UV-preionization used in the present 3-atm ATF CO_2 amplifier, has advantages for large-aperture high-pressure discharge applications. Because of strong absorption of UV radiation by CO_2 molecules, UV predionization is difficult to implement even for $dP > 25$ cm.atm (e.g., P=5 atm and d=5 cm). The penetration range for 30-50 keV x-rays is much larger. Another important advantage of x-ray preionization is the elimination of spark discharges associated with UV preionization method which contribute significantly to the dissociation of CO_2, thus shortening gas lifetime.

With relatively simple corona-cathode e-guns, collimated "sheets" of x-rays with the cross-section of 0.1 m^2 or more can be readily produced. At applied ~100 kV cathode voltage, the e-beam with the current density of ~1 A/cm^2 maintained during ~1 μs is adequate to generate in the interelectrode space the initial photoelectron concentration of ~10^8 cm^{-3} necessary for starting a uniform volumetric discharge at $dP \approx 50$-100 cm.atm.

After the choice on the preionization mechanism, the next key decision would be regarding the discharge parameters. The high-voltage pulse power supply to the discharge shall comply with requirements to the breakdown and sustain potentials set by parameters d, P, and ξ. Based on available data, we can draw a semi-empirical law for the reduced sustain voltage, V_s/dP, depending upon ξ - proportion of the molecular components in the CO_2:N_2:He mixture:

$$V_s/dP[\text{kV/cm.atm}] = 2.5(1+0.1\xi[\%]) \qquad (6)$$

resulting in V_s/dP=6 kV/cm.atm @ ξ=15%. It also turns out that the breakdown voltage is less than 2 times above the sustain voltage (e.g., it is ~10 kV/cm.atm @ ξ=15%). The pulser suitable to sustain discharge at given d, P, and ξ parameters is automatically good to produce a breakdown at the open circuit conditions. As follows from Eq.(6), a technically feasible pulse generator with the output voltage of 1 MV is capable to maintain discharge in ξ=15% mixture at dP=80 cm.atm.

For given V and ξ, the product dP is invariant defined by Eq.(6). As we discussed previously, the pressure increase leads to higher peak power output because of the higher specific stored and extractable energy and shorter laser pulse duration. As high as 10 atm pressure is required to amplify 10-ps laser pulse. Multi-isotope gas mixture gives the possibility to reduce the pressure. As short as 3-ps laser pulse may be amplified at 5 atm pressure. This and other practical considerations limit maximum d value to ≤10 cm.

The electrical energy deposition into the discharge, E_{dep}, needed to attain a gain of ~3%/cm can be estimated by the semi-empirical requirement

$$E_{dep}[\text{kJ}] \geq 0.12 PSd[\text{atm}.l]. \tag{7}$$

That results in $E_{dep} \geq 10$ kJ required to energize the discharge at the 10 l volume and 10 atm pressure.

Glow discharge is a transient phenomenon at $P \geq 0.1$ atm, and contracts into streamer channels during the time interval that decreases inversely proportional to the gas pressure. While the desirable discharge duration should be less than the onset of instabilities and the gain depletion time, it should be also high enough to permit an efficient transfer of the excitation from N_2 to CO_2 molecules. In combination, these requirements set the optimum discharge duration at

$$\tau_{10\text{-}90}[\mu\text{s}] \approx 3/P[\text{atm}]. \tag{8}$$

Here we define the discharge duration as the time interval when 80% of the stored electric energy is deposited into the discharge. For impedance-matched discharges,

$$\tau_{10-90} \approx 2\sqrt{LC_{sh}}, \tag{9}$$

where L is the inductance of the discharge circuit and C_{sh} is the shock capacitance of the high-voltage pulser. Equation $E_{dep}=C_{sh}V_{out}^2/2$ completes the set of self-consistent equations that define the primary parameters of the high-pressure big-volume amplifier for the psTW-CO_2 laser system, Eq.(6-9), that are compiled in Table 2.

Cross-section diagram of the high-pressure x-ray preionized amplifier designed for the ATF terawatt CO_2 laser system are shown in Fig.3. X-rays penetrate into the active volume of 100×10×8 cm^3 through the mesh ground electrode and Be window that separates the vacuum x-ray tube from the high-pressure discharge volume. The big, 10×8 cm^2, optical aperture of the amplifier helps to accommodate the regenerative amplifier and subsequent multipass amplification in a single discharge cell. This permits a reasonably compact design of the terawatt laser system. The collimated laser beam will be transported to the experimental hall and interact with a picosecond 70-MeV, 1-nC electron bunches to test various laser acceleration schemes. The psTW-CO_2 laser system with parameters summarized in Table 2 is expected to be operational in 1997.

III. Laser Accelerator Schemes with Picosecond CO_2 Laser Driver

All the variety of the laser accelerator schemes proposed so far may be split into three major categories: far EM field, near EM field, and plasma accelerators. How to define the border between the first two methods? EM field may be presented as a sum of propagating EM waves

$$\vec{E}(\vec{r},t) = \sum_j A_j \exp[i(\vec{k}_j \times \vec{r}_j - \omega_j t)]. \tag{10}$$

When all wave vectors $\vec{k}_j$ are real, we talk about far field accelerators. For these schemes it is essential that any distances from the source of the field or from any boundary surface are >>λ. Otherwise, near field effects come into play.

Fields with imaginary $\vec{k}_j$ are called near fields. Actually, in this case, we talk about evanescent fields vanishing within a λ-thick layer above the surface.

In the third group of methods, particles are accelerated not by EM fields directly but by electrostatic fields due to the charge separation in laser-induced plasma waves.

The study of any scheme has the primary practical goal of finding an alternative to conventional accelerators in order to build, in the future, more economical high-energy (~TeV) machines, or compact moderate-energy (~GeV) accelerators. So far, the record of ~100 MeV over the 0.5 cm distance laser acceleration has been demonstrated using the SMLWFA method[21]. Presently, a variety of acceleration methods are under consideration and study.

At the ATF, two far-field accelerator experiments are currently active; these are: ICA[9] and IFEL[11] accelerators. In addition to it, a near field Grating Linac[22] is scheduled for tests, and a plasma acceleration experiment is considered for initiation[7,23]. We discuss here how all these schemes can benefit from using the terawatt picosecond CO_2 laser that is presently under construction.

III.1 Far Field Accelerators

III.1.1 Inverse Cherenkov Accelerator

In any laser acceleration scheme, the key question is how to maintain synchronism between particles and oscillating electric fields over an appreciable distance. One of the possibilities is when the particle, traveling in medium with velocity βc, is intersected by the EM wavevector at the Cherenkov angle, θ, which is described by the condition

$$\cos\theta = \beta n^{-1}. \tag{11}$$

Here, the inclination of the wavevector is responsible for developing a longitudinal accelerating field, while the medium produces retardation of the phase velocity of the wave to match the speed of electrons. Inverse Cherenkov acceleration is the only example of a first order, far field acceleration process where the particle interacts with a single EM wave.

In the first ICA demonstration at Stanford University[24], a linear polarized, focused Nd laser beam crossed the path of electron beam in the interaction cell filled with hydrogen. The observed energy shift was 50 keV over the 7 cm interaction length.

In a modified scheme[8] (see Fig.4) which is under test at the ATF, we start with a radially polarized beam. By an axicon, the laser beam is converged to the e-beam axis, z, producing a cylindrically symmetrical interference pattern. An amplitude of the longitudinal component of the electric field, which is responsible for electron acceleration, is described analytically by Bessel function of the first kind of the order 0:

$$E_z(r,z) = tg\theta \times E_0(z) J_0(2\pi\theta r/\lambda), \tag{12}$$

where $E_0(z)$ is a field amplitude that depends upon the laser intensity distribution at the axicon surface, $W(R)$,

$$E_0(z) = 2\pi\theta\sqrt{\frac{2zW(R)}{\varepsilon_0 c\lambda}} \tag{13}$$

with z related to R by $z=R/\theta$. The distribution described by Eq.(12) has the maximum along the z axis that defines the acceleration gradient attainable under the phase matching condition, Eq.(11). The radial position of the first minimum in the distribution Eq.(12) is observed at

$$r_{min}=0.38\lambda/\theta; \tag{14}$$

for λ=10.6 μm and θ=20 mrad, $r_{min}\approx$200 μm. In a practice, the parameter r_{min} shall be chosen according to the realistic size of the e-beam, $r_{min}\approx r_e$, that propagates along the axicon axis. Then, as follows from Eq.(14), the longer λ permits to choose the proportionally bigger angle θ.

Combining this condition with Eqs.(12,13), we come to the conclusion that $E_z \sim \lambda^{3/2}$ is ultimately due to the stronger inclination of the laser wavefront to the e-beam propagation.

Another advantage of using the relatively long-wavelength CO_2 laser radiation for the ICA scheme is due to the increase of the "phase slippage" distance, L_{slip}, where the accelerating particle stays in partial synchronism with the driving EM field. The expression for L_{slip} comes from the condition $t_{slip}\Delta v_e = \lambda/2$ with $t_{slip} = L_{slip}/c$ and $\Delta v_e = \Delta\beta c$, where $\Delta\beta$ is due to the electron acceleration above the β-number defined by Eq.(11). Using $\beta = \sqrt{1-1/\gamma^2}$, we derive

$$L_{slip} = \frac{\lambda\gamma^3}{2\Delta\gamma}. \qquad (15)$$

For example, for the conditions of the ATF ICA experiment, L_{slip}=20 cm at $\Delta\gamma$=25 that corresponds to 12.5 MeV electron acceleration. It becomes evident that 1-μm laser would require much stronger acceleration gradient in order to attain similar net acceleration over the 10 times reduced distance. However, that would be difficult to satisfy considering the above mentioned proportionality $E_z \sim \lambda^{3/2}$.

Fig.5 presents the snap shots from the electron energy spectrometer positioned downstream from the ICA gas cell. Since the electron bunch length is much longer than the laser wavelength, the interaction between the e-beam and the laser beam occurs over all phases of the EM wave, resulting in both accelerated and decelerated electrons. The spectrometer has a momentum acceptance range of ~±2% of the mean energy. Since the ICA interaction results in larger energy modulation, the spectrometer has been scanned to obtain the complete spectrum. Up to 3.7 MeV maximum acceleration has been measured when ~1 GW CO_2 laser power was delivered to the interaction region.

After the completion of the ongoing ATF CO_2 laser upgrade to a 3 ps pulse duration, up to 200 GW laser peak power may be delivered into the hydrogen cell before gas breakdown or optics damage occurs. Monte-Carlo computer simulation of the ICA process shows a possibility of a 100 MeV acceleration demonstration over the 30 cm long interaction range.[25,26] The acceleration efficiency may be improved by better phasing of the electrons with the peak accelerating field. For this purpose, periodical electron prebunching with the spatial interval equal to the laser wavelength will be produced in a low-laser-power IFEL accelerator section placed before the high-power ICA accelerator cell. Fig.6 illustrates the predicted enhanced efficiency when prebunched e-beam is accelerated in a single-stage Inverse Cherenkov Accelerator.

III.1.2 Inverse FEL Accelerator

The IFEL scheme is an example of a second order, far field laser acceleration process. In this case, a second field of a wiggler magnet is used to bring the relativistic particles into a transverse oscillating motion. Thus, transverse EM laser field has a projection of its electrical component along the local direction of the e-beam propagation (see Fig.7). Hence, electric forces may produce an additional kick to the electrons in the direction of their propagation, provided the laser field is in phase with the electron wiggling.

In vacuum, the oscillating electron can not propagate with a phase velocity of light along the direction of the laser beam. Now, synchronism means that the electron should slip exactly one period (or integer number of periods) of the EM wave while traveling a wiggler period, λ_w. The synchronism condition at a small angle limit takes the form

$$\lambda = \frac{\lambda_w}{2\gamma^2}(1+K^2) \qquad (16)$$

where K is a dimensionless wiggler parameter equal to $K = \frac{eB_w\lambda_w}{2\pi mc^2}$ and B_w - wiggler magnetic field. Hence, the condition Eq.(16) may be satisfied by adjusting wiggler field and period.

A reasonable estimate of the energy gain by the electron beam in a wiggler of length L_w is given by

$$\Delta E = \frac{eE_L}{2\gamma_{in}} Kf(K)L_w \sin\psi_r, \tag{17}$$

where E_L is the laser electric field amplitude, γ_{in} is the initial electron energy relativistic factor, ψ_r - the resonance phase ($\approx 45^o$ for maximum bunch size), and $f(K)\approx 0.4$.

First proposed in 1972,[10] IFEL acceleration has been demonstrated using FEL[27] and a moderate-power CO_2 laser[28] as a driver.

The goal of the ATF IFEL experiment is further optimization of the accelerator parameters at a higher CO_2 laser power. The laser beam is guided inside a low-loss sapphire waveguide of a 2.8 mm diameter mounted inside the 0.5 m-long wiggler. This concept may be also relevant to the future multi-stage IFEL accelerators.

Fig.8 presents electron energy distributions obtained during the ATF IFEL experiment. We see that practically all the electrons are trapped and accelerated. Because of problems with vacuum degradation when the laser is delivered inside the guide, the laser power has been kept below 0.5 GW. Observed acceleration is 2.2%. Further optimization is under way.

Near term plans call for increasing the CO_2 laser power to 200 GW. This should result in the accelerating gradient of ~100 MeV/m.

III.2 Near Field Accelerators

III.2.1 Grating Linac

Near-field laser accelerator scheme illustrated by Fig.9 is based on excitation of an evanescent surface field when a laser beam is cylindrically focused onto a periodic structure. Electrons injected parallel to the surface will be accelerated when moving in phase with standing wave oscillations. This process is similar to what is observed in the RF linac, and is therefore this scheme is known as a Grating Linac[12]. For a relativistic e-beam to satisfy the synchronism conditions, the structure period is nearly equal to the laser wavelength. Thus, a long-wavelength CO_2 laser radiation helps to use reasonably "macroscopic" structures. Photographs of two possible structures produced by a lithographic etching technique are presented in Fig.10. Taking into account that the evanescent accelerating field is observed within one wavelength distance from the surface, the requirement to the electron beam dimensions are also not as severe as would be with the 1-μm laser driver. In addition, the reduced phase slippage at a long wavelength is relevent for this scheme as well.

When a 1 GW CO_2 laser beam is focused to the 5×0.03 mm strip at the "foxhole" structure shown in Fig.10, 1 GeV/m acceleration is predicted[29]. Using a short, picosecond laser pulse is a way to avoid the optical damage of the structure. To ensure the interaction of the e-bunch directed perpendicular to the laser beam over the appreciable acceleration distance (much longer than the laser pulse length), a linear delay shall be introduced across the laser intensity front. It may be done by reflecting the laser beam from the diffraction grating prior to cylindrical lensing.

III.2.2 Dielectric-Loaded Resonant Laser Accelerator

In another proposed near-field electron accelerator scheme, linearly polarized laser radiation penetrates through the periodically modulated dielectric structure filling the gap of the

Fabry-Perot interferometer as shown in Fig.11[13]. At the high quality factor of the interferometer cavity, Q, which is actually equal to the number of the optical double passes required to reach the field saturation in the cavity, a large stored EM energy and field amplitude can be obtained at relatively low input laser power. Periodic modulation of the permittivity, ε, within the dielectric masks sandwitched between the reflective layers of the interferometer

$$\varepsilon(z)= \varepsilon_0 + \Delta\varepsilon \cos(2\pi z/\lambda) \tag{18}$$

ensures a space-periodical modulation of the field phase in the central vacuum gap, provided the gap width is of the order of the laser wavelength. The electron beam, propagating inside the vacuum gap in the direction of the laser beam polarization, experiences acceleration due to the synchronously oscillating electric field. The average accelerating field is

$$\overline{E}_z \cong \sqrt{\frac{4\pi QI}{(1+\Delta\varepsilon^2/2)}}, \tag{19}$$

where I is the incident laser intensity. The accelerating field in excess of 1 GV/m has been estimated for the realistic experimental parameters.

Similar to Grating Linac, this scheme looks more practical with the relatively long-wavelength CO_2 laser, provided the problem of laser damage of the structure is solved.

III.3 Laser-Driven Plasma Accelerators

It looks logical to use a high-power CO_2 laser, which is a strong ionizer, in the schemes where such ionization and related effects are not problems but are desirable, as it happens in plasma accelerators.

As illustrated in Fig.12, an EM wave packet propagating in plasma ponderomotively separates charges initiating their oscillation at the plasma eigenfrequency, ω_p, that depends upon the electron density, N_e, by

$$\omega_p = 2e(\pi N_e/m)^{1/2}. \tag{20}$$

Plasma wave follows the laser pulse with a phase velocity equal to the group velocity of the laser pulse, $v_{ph} = v_{gr}^L = cn$, where $n = (1-\omega_p^2/\omega^2)^{1/2}$ is a plasma refractive index.

A relativistic particle propagating together with plasma wave will experience acceleration until it slips out of synchronism over the distance

$$l_a \approx \lambda_p(\omega/\omega_p)^2. \tag{21}$$

Started from oscillation of free plasma electrons in the laser field, amplitude of a plasma wave is related to the energy of the electron oscillatory motion called ponderomotive potential

$$W_{osc} = e^2E_L^2/2m\omega^2, \tag{22}$$

where E_L is the laser field amplitude. This quadratic dependence of the ponderomotive potential upon the laser wavelength makes CO_2 laser an attractive candidate to drive plasma accelerator.

Amplitude of the accelerating field due to the longitudinal charge separation depends also upon the particular method of the plasma wave excitation.

In the Laser Wakefield Accelerator (LWFA) scheme (Fig.13a), we initiate plasma oscillations by a strong and brisk "shock" that is produced with a short laser pulse optimally equal to the half-period of the plasma wave $\tau_L = \lambda_p/2c$. Note, that after developing a TWps-CO_2 laser, there will be the first-time opportunity to use CO_2 laser in this scheme in a practically interesting range of a plasma density, N_e=10^{14}-10^{15} cm^{-3}. The advantage of using CO_2 laser in the LWFA scheme stems from the proportionality of the accelerating field to the laser

wavelength that is the result of the strong ponderomotive potential in the CO_2 laser field and, in particular, follows from the expression[6]

$$E_a = (\pi^2 mc^2 / e)a^2 / 4\lambda_p (1 + a^2/2)^{1/2}, \tag{23}$$

where

$$a \equiv eE_L / m\omega c \tag{24}$$

is the unitless laser strength parameter.

In the Laser Beat Wave Accelerator (LBWA) scheme (see Fig.13b) we choose periodical force that matches the plasma frequency and resonantly enhances the plasma oscillations. Such modulation of the acting laser intensity is produced by mixing two laser beams of different frequencies that satisfy a condition $\omega_1 - \omega_2 = \omega_p$.

The accelerating field reaches for the LBWA cofiguration an amplitude of

$$E_a = (5a_1 a_2)^{1/3} N_e^{1/2}. \tag{25}$$

Thus, due to the proportion of $E_a \propto \lambda^{2/3}$ (see Eq.(24) and (25)), CO_2 laser can produce 6 times stronger acceleration than a 1-μm laser of the equal intensity.

The third, Self-Modulated LWFA scheme (Fig.13c), looks the most promising. It comes to the scene when the laser pulse is relativistically strong. Relativistically strong means that laser power, P, satisfies the condition of relativistic self-focusing (RSF)

$$P \geq 17(\omega/\omega_p)^2 [GW]. \tag{26}$$

In this case, initially small plasma density oscillations cause modulation at the plasma frequency of the laser beam envelope and its intensity. Then, the pulse resonantly enhances the plasma oscillation similar to the LBWA scheme matched automatically to the local plasma density. It is understood that the laser pulse length in this case shall extend over several plasma periods, $\tau_L \rangle\rangle 2\pi / \omega_p$.

It has been shown by simulations that, if the laser pulse is just strong and long, it is still not enough to produce an intense and regular wake[7]. The wake needs an efficient initiation, similar to that provided in the LBWA or LWFA schemes. Fig.13c illustrates one of the possibilities where a steep leading front, with $\tau_{fr} < \lambda_p / c$, serves as a good initiator for a plasma wave. Simulations done for a 5-TW, 1.5-ps, properly shaped CO_2 laser pulse propagating in a plasma channel[7] predict electron acceleration to 500 MeV (see Fig.14).

Finally, let us address the question of how to compare potential performance of 10-μm and 1-μm lasers in the SMLWFA configuration. An accelerating field attainable with the SMLWFA scheme at the plasma wave breaking limit is

$$E_a \propto \omega a^2 / \sqrt{1 + a^2/2}. \tag{27}$$

According to Eq.(24), for fixed laser field, a is proportional to λ. In spite of this fact, the expression for the net acceleration (see Eq.(21))

$$\gamma_{max} \approx a(\omega/\omega_p)^3 \tag{28}$$

still seems beneficial for shorter wavelength lasers. However this first impression is misleading. The thing is that we are not free in making the choice for parameters entering Eq.(28). The values of ω and ω_p are interrelated through the self-focusing condition, Eq.(26).

Assume for our wavelength comparison laser beams of the equal power both close to the self-focusing condition and focused to the equal spot size. Then, the ratio ω/ω_p is equal for any laser wavelength. The result of it is that the maximum acceleration is proportional to λ, $\gamma_{max} \propto P^2 / \omega$. When λ=1 μm, we need to channel the laser beam and, hence, e-beam in a 10 μm waveguide in order to obtain similar acceleration as with a CO_2 laser beam inside a 100 μm waveguide. Doing it, we may encounter severe problems with the electron beam scattering.

When we increase ω and ω_p 10 times, the plasma density will be increased 100 times according to Eq.(20), with the proportional increase of the multiple scattering in the gas described by

$$\Delta\theta_{1/e} = (W_s/W)(z/L_R)^{1/2}[1+0.1\log_{10}(z/L_R)] \quad (29)$$

where $\Delta\theta_{1/e}$ is the angular spread of the e-beam, W[MeV] is the mean electron energy, W_s=19.7 MeV is a multiple scattering constant, z is the path length through the gas traversed by the electron, and L_R is the radiation length of the medium, which for hydrogen gas is $L_R=7\times10^5$[cm]/p[atm].[30] The result of gas scattering is the e-beam emittance growth and reduced acceleration efficiency due to a poor overlap of the expanded e-beam with the narrow channeled laser beam. A simplified formula for the e-beam radius growth due to the multiple scattering

$$\Delta r(z) = \frac{2}{3}\frac{W_s}{W\sqrt{L_R}}z^{3/2} \quad (30)$$

indicates that the e-beam expands by 10 μm in radius after passing a 2 cm distance in a 0.25 atm of H_2.

It follows that the CO_2 laser, which permits similar acceleration at 10 times wider waveguide and e-beam diameters and a 100 times lower pressure, looks more attractive for prospective high-energy plasma accelerator.

Considering the feasibility of conducting a sub-GeV plasma acceleration experiment at the ATF, we should remember that not just a terawatt CO_2 laser will be available for this purpose, but also one of the world's brightest e-beams that may be fitted inside a 100-μm wide channel.

IV Plasma Channeling with CO_2 Lasers

IV.1 Principle of Plasma Channeling

High intensity required to achieve strong accelerating field in a plasma accelerator presumes sharp laser focusing. However, the short Rayleigh length limits the effective interaction length and, thus, the net acceleration. Waveguiding may help to maintain a high laser intensity over the appreciably long distance.

Let us characterize first the conditions for waveguiding. Consider a collimated laser beam propagating in a medium with a refractive index, n. In order to compensate for natural divergence of the beam, the medium should act as a distributed focusing lens. This means that the phase velocity of the beam, $v_p=c/n$ shall be profiled in the medium according to the condition $\partial v_p/\partial r>0$. The way to do this is to introduce a radial drop of the refractive index ($\partial n/\partial r<0$).

For application in particle accelerators, only a low density gaseous medium may be practical. However, because of the small gas refraction, a high increase of the gas density at the beam axis would be required to produce an appreciable lens effect. In a plasma, we have an opposite situation. Its refractive index is relatively strong and drops with the electron density, N_e, increase according to Eq.(3). Hence, plasma appears to be the most promising substance for optical channeling.

For $N_e<<N_{cr}$, Eq.(3) takes the form

$$n = n_0(1-e^2\lambda^2 N_e/2\pi c^2 m). \quad (31)$$

It follows that the condition $\partial n/\partial r<0$, required for waveguiding, may be satisfied in two ways: (a) by profiling the electron density as $\partial N_e/\partial r>0$, or (b) using the relativistic growth of the electron mass, m, due to the ponderomotive electron motion induced by the laser field. Method (a) formulates the basics of laser guiding in plasma channels discussed in the present section. Effect

(b) is responsible for RSF[31] experimental observations of that have been reported recently[32]. It has been proposed however, that, due to the inherent RSF instability, this process by itself can not confine the laser beam in a regular manner over an appreciably long distance[33-35]. The preformed plasma channels, in combination with RSF or taken alone, may help to control the extended confinement of the laser beam in plasma.

If the plasma density increases in a radial direction, refractive index drops according to the equation

$$\frac{\Delta n}{n_0} = -\frac{\Delta N_e}{2N_{cr}} \tag{32}$$

that follows from Eq.(3). When the refractive index drop satisfies conditions for total internal reflection, light will propagate like inside the fiber. For an electromagnetic wave incident onto the plasma layer at the angle β_0 as shown in Fig.15, the condition for reflection is

$$n(r) \le n_0 \sin\beta_0 \tag{33}$$

or for oblique incidence $n(r) - n_0 \equiv \Delta n(r) \le -n_0\theta_0^2/2$ and

$$\Delta N_e \ge N_{cr}\theta_0^2. \tag{34}$$

If we consider a cylindrical plasma layer, for a focused Gaussian beam with a diffraction divergence

$$\theta_0 = \frac{\lambda}{\pi w_0}, \tag{35}$$

the condition for optical guiding is

$$\Delta N_e \ge \frac{mc^2}{\pi e^2 w_0} \equiv (\pi r_e w_0^2)^{-1}. \tag{36}$$

Here, r_e=2.82×10^{-13} cm is the classic electron radius.

For example, a Gaussian laser beam focused into a spot with a radius of w_0=100 μm, will be trapped in a plasma waveguide with a "wall height" of ΔN=1.5×10^{16} cm^{-3}. Note that this condition does not depend upon the laser wavelength.

IV.2 Plasma Waveguides with Axicon-Focused Laser Beams

Two methods to produce plasma channels look feasible (see Fig.16). Both of them are based on using axicon focused laser beams. In the first method[4], a linearly polarized beam focused by the axicon produces a circularly symmetric interference pattern along the axicon axis described by the J_0 Bessel function (see Fig.16a). Hence, the laser field is not profiled to produce the $\partial N_e/\partial r>0$ distribution immediately via direct ionization.

To understand the processes leading to the plasma channel formation using J_0-shaped intensity distribution, let us address the diagram presented in Fig.17.

At the first stage of the process, plasma is produced along the z-axis by tunneling and avalanche ionization.

Intense plasma heating within the narrow region near the axis results in a local temperature increase (typically, up to ~50,000 ^{o}K) and the proportional adiabatic pressure jump that generates a cylindrical detonation wave expanding with a supersonic velocity outwards. Behavior of such a wave is similar to the propagation of high-current discharges or explosive combustion waves and has been extensively studied previously[36]. A shock wave, pushing the gas as a supersonic piston, produces a discontinuity of much higher amplitude than the ambient gas density and leaves a rarefied channel behind. Typical distributions of the gas density, ρ, and temperature in a shock wave are sketched in Fig.17c. The superposition of ρ and T distributions explains a characteristic

electron density distribution shown in Fig.17d that features a positive gradient $\partial N_e/\partial r>0$ desired for waveguiding. Optical waveguiding under these conditions has been already demonstrated.[4]

Another similar method uses a radially polarized laser beam to form a J_1 Bessel distribution[5] (see Fig.16b). This provides a field naturally shaped with interferometric precision to produce gas ionization appropriate for waveguiding. The radial position of the first maximum occurs at

$$r_{max}=0.29\lambda/\theta_c \qquad (37)$$

and is equal to 170 μm for a representative case of λ=10.6 μm and θ_c=20 mrad.

The next step is to convert this favorably shaped electric field into the corresponding cylindrical plasma density distribution by means of gas ionization. We consider a cascade ionization mechanism that requires relatively low level of laser irradiation. The characteristic rate of plasma formation has a quadratic dependence upon ω. This means that using a CO_2 laser, 100 times less intensity is required to produce the same avalanche ionization effect as compared with a Nd laser[5]. A method for generating a radially polarized CO_2 laser beam and its focusing by an axicon mirror has been demonstrated during the course of the ICA experiments[9].

Still another relatively simple way of optical channeling inside a dielectric capillary, experimentally studied in Ref.[37] with a picosecond terawatt Nd:YAG laser, is also of a consideration for the psTW-CO_2 laser beam confinement in underdense plasma.

V. Conclusions

Variable picosecond and even subpicosecond CO_2 laser pulses with a contrast of 10^5-10^6 and a peak power ~1 MW may be readily produced by the optical semiconductor switching method. To avoid severe pulse expansion in the course of amplification, high-pressure, multi-isotope laser amplifier shall be used to bring the switched pulse to the terawatt level. Following this approach, the first terawatt picosecond CO_2 laser is under construction at the ATF.

There are several reasons why we are interested in using a CO_2 laser for particle acceleration. With far-field accelerators, we may benefit from a slow phase slippage. For near-field accelerators, the CO_2 laser helps to use macroscopically-sized structures and e-beams. With plasma accelerators, we capitalize on the strong ponderomotive potential of electron oscillating in the laser field and all outcomes of it such as: strong plasma wave formation, relativistic self-focusing at a low plasma density, etc.

We intend to utilize all above-listed features of the psTW-CO_2 laser to benefit the laser acceleration experiments at the ATF. So far, high-brightness, 10-ps, 50-MeV electron bunches have been accelerated to several MeV at the ATF with ~1 GW CO_2 laser pulse using far-field accelerator schemes. Due to the expected acceleration scaling as a square root of the laser power, 100 MeV ICA and IFEL demonstration is possible after the laser upgrade. Combined IFEL-ICA experiment is under preparation to enhance the acceleration efficiency by the electron periodical prebunching at the laser wavelength.

Laser linac near-field accelerator experiment is scheduled for tests.

By laser wake field accelerator method, 500 MeV acceleration over a 4-cm distance is feasible when using the properly shaped 5-TW laser pulse guided in a plasma channel.

Acknowledgments

The author wishes to thank I. Ben-Zvi for stimulating discussions, J. Skaritka and colleagues who helps in developing a terawatt picosecond CO_2 laser, S. Bulanov for theoretical and computational support of the laser wake field accelerator design. The success of the ATF laser accelerator experiments, reviewed in this paper, is due to the team work of scientific and technical personal of the ATF and associates. Principal investigators on these experiments are: A. vanSteenbergen (IFEL) and W. Kimura (ICA).

The work is supported by the US Department of Energy.

References

1. M. Everett, A. Lal, D. Gordon, C. Clayton, K. Marsh, C Joshi, *Nature*, **368**, 527 (1994)
2. N.A. Ebrahim, *J. Appl. Phys.*, **76**, 7645 (1994)
3. T. Tajima and J.M. Dawson, *Phys.Rev. Lett.*, **43**, 267 (1979)
4. C.G. Durfee III and H.M. Milchberg, *Phys. Rev. Lett.*, **71**, 2409 (1993)
5 I.V. Pogorelsky, W.D. Kimura, and Y. Liu, *Proc. Advanced Accelerator Concepts*, June 12-18, 1994, Fontana, WI, AIP Conference Proceedings, **335**, 419 (1995)
6. J. Krall, A. Ting, E. Esarey, and P. Sprangle, *Proc. of PAC*, May 17-21, 1993, Washington, DC, 2629 (1993)
7. S.V.Bulanov, T.J. Esirkepov, N.M. Naumova, F. Pegoraro, I.V. Pogorelsky, and A.M. Pukhov, "Controlled Wakefield Acceleration via Laser Pulse Shaping", *IEEE Trans. on Plasma Sci.*, **24**, 393 (1996)
8. J.R. Fontana and R.H. Pantell, *J. Appl. Phys.*, **54**, 4285 (1983)
9. W.D. Kimura, G.H. Kim, R.D. Romea, L.C. Steinhauer, I.V. Pogorelsky, K.P. Kusche, R.C. Fernow, X. Wang, and Y. Liu, *Phys. Rev. Lett.*, **74**, 546 (1995)
10. R.B Palmer, *J. Appl. Phys.*, **43**, 3014 (1972)
11. A. Fisher, J. Gallardo, J. Sandweiss, and A. vanSteenbergen, *Proc. Advanced Accelerator Concepts*, Port Jefferson, NY, 1992, AIP, **279**, 299 (1993)
12. R.B. Palmer, *Proc. Laser Acceleration of Particles*, AIP., **91**, 179 (1982)
13. J. Rosenzweig, A. Murokh, and C. Pelligrini, *Phys. Rev. Lett.*, **74**, 2467 (1995)
14. V.T. Platonenko and V.D. Taranukhin, *Sov. J. Quant. Electron.*, **13**, 1459 (1983)
15. P.B. Corkum, *IEEE J. Quant. Electron.*, **QE-21**, 216 (1985)
16. P.B. Corkum and D. Keith, *J. Opt. Soc. Am.*, **B2**, 1873 (1985)
17. A.Y. Elezzabi, J. Meyer, M.K.Y. Hughes, and S.R. Johnson, *Opt. Lett.*, **19**, 898 (1994)
18. I.V. Pogorelsky, J. Fischer, K. Kusche, M. Babzien, N.A. Kurnit, I.J. Bijio, R.F. Harrison, and T. Shimada, *IEEE J. Quant. Electron.*, **31**, 556 (1995)
19. I.V. Pogorelsky, "ATF CO_2 Laser System Upgrade to Terawatt Peak Power", Preprint BNL-61859 (1995)
20. I.V. Pogorelsky, W.D. Kimura, C. Fisher, and N. Kurnit, *6th Workshop on Advanced Accelerator Concepts*, June 12-18, 1994, Fontana, WI, AIP Conference Proceedings, **335**, 405 (1995)
21 A. Madena, Z. Najmudin, A.E. Dangor, et.al., *Nature*, **377**, 606 (1995);
T. Katsouleas, "Laser Acceleration of Electrons in Plasmas", Joint Meeting of APS and AAPT, May 2-5, 1996, Indianapolis, IN
22. R.C. Fernow and J. Claus, *Proc. Advanced Accelerator Concepts*, Port Jefferson, NY, 1992, AIP, **279**, 212 (1993)
23. I.V. Pogorelsky, "Relativistically Strong CO_2 Laser Driver for Plasma-Channeled Particle Acceleration", to be published in *Proc. Lasers'95*, December 4-8, 1995, Charleston, SC

24. J.A. Edighoffer, W.D. Kimura, R.H. Pantell, M.A. Piestrup, and D.Y. Wang, *Phys. Rev.*, **A23**, 1848 (1981)
25. R.D. Romea and W.D. Kimura, *Phys.Rev.*, **42D**, 1807 (1990)
26. W.D. Kimura, R.D. Romea, and L.C. Steinhauer, *Particle World,* **4**, #3, 22 (1995)
27. I. Wernick and T.C. Marshall, *Proc. Advanced Accelerator Concepts*, Port Jefferson, NY, 1992, AIP, **279**, 292 (1993)
28. A.T. Amatuni et al, *Part. Accel.*, **32**, 221 (1990)
29. R.C. Fernow and J. Claus, *Proc. Advanced Accelerator Concepts*, Port Jefferson, NY, 1992, AIP, **279**, 212 (1993)
30. V.L. Highland, *Nuclear Instruments and Methods*, **129**, 497 (1975)
31. P. Sprangle, E. Esarey, and A. Ting, *Phys. Rev.*, **41A**, 4463 (1990)
32. G. A. Mourou, "Impact of T^3 Lasers in Laser Acceleration"; K. Nakajima, "Challenge to a Table-Top High-Energy Wakefield Accelerator", both at *37th Annual Meeting of the Division of Plasma Physics APS*, Nov. 6-10, 1995, Louisville, Kentucky
33. P. Sprangle, E. Esarey, J. Krall, and G. Joyce, *Phys. Rev. Lett.*, **69**, 2200 (1992)
34. C.D. Decker, W.B. Mori, and T. Katsouleas, *Phys Rev.*, **50E**, R3338 (1994)
35. G.A. Askar'yan, S.V. Bulanov, F. Pegoraro, and A.M. Pukhov, *JETP Lett.*, **60**, 251 (1994)
36.. Yu. P. Raizer, "Laser-Induced Discharge Phenomena", Consultants Bureau, New York and London, 1977
37. S. Jackel, R. Burris, J. Grun, A. Ting, C. Manka, K. Evans, and J. Kosakowskii, *Opt. Lett.*, **20**, 1086 (1995)

Tables

Table 1. Typical Parameters of Solid State and CO_2 Lasers

PARAMETER	Solid State	10-atm CO_2
Bandwidth (THz)	5-50	1
Cross section ($\times 10^{-20}$ cm^2)	1-30	5
Gain (%/cm)	~50	3-4
Saturation energy (J/cm^2)	1-20	0.5
Breakdown threshold (J/cm^2)	1	3
Stored energy (J/cm^3)	1	0.01
Active volume (cm^3)	10-100	10,000
Gain relaxation time (μs)	>1	0.2
Repetition rate limit (Hz)	1-10	100-1000
Average power limit (W)	1-10	100-1000

Table 2. ATF CO_2 Laser and e-Beam Parameters

CO_2 Laser (Present)	
Oscillator Peak Power [MW]	1
Oscillator Pulse Duration [ns]	100
Switched Pulse Duration [ps]	~300
Double Sliced Pulse Duration [ps]	10-300
Amplified Pulse Duration [ps]	100
Output Energy [J]	1
Output Peak Power [GW]	10
Repetition Rate [Hz]	0.1
CO_2 Laser (Upgrade)	
Amplified Pulse Duration [ps]	3-50
Output Energy [J]	3-30
Output Peak Power [TW]	~1
Repetition Rate [Hz]	0.1
LINAC	
Electron Energy [MeV]	50-70
Peak Current [A]	50
Bunch Duration FWHM [ps]	10
Repetition Rate [Hz]	3
Normalized Emittance [mm.mrad]	2
Electron Momentum Spread [relative]	0.2%

Figure Captions

Fig.1 Principle optical diagram of the picosecond slicing set-up

Fig.2 Principle optical diagram of the psTW-CO_2 laser system

Fig.3 Cross-sectional diagram of the x-ray preionized CO_2 laser amplifier

Fig.4 Axicon focusing of radially polarized laser beam in the Inverse Cherenkov Accelerator

Fig.5 Snap-shots of the electron spectrometer screen without laser (a) and with ~1-GW laser pulse delivered to the ICA cell (b)

Fig.6 Monte-Carlo computer simulation for Inverse Cherenkov acceleration of prebunched electrons: initial electron energy 50 MeV, CO_2 laser power 50 GW, Cherenkov angle θ=20 mrad, interaction length 20 cm[25]

Fig.7 Principle diagram of the IFEL accelerator

Fig.8 Electron beam distributions obtained on a phosphor screen placed downstream of the dipole bending magnet at the end of the IFEL beamline:(a) no laser; (b) with 0.5 GW laser power; E(linac)=40 MeV, B_w=10 kG, λ_w=2.9-3.1 cm

Fig.9 Principle diagram of the grating linac

Fig.10 Examples of the 10-μm period structures for the grating linac[22]

Fig.11 Schematic of the top half of one period of a dielectric loaded laser resonant acceleration structure[13]

Fig.12 Laser excited plasma wake:a) wave packet ponderomotively separates charges; b) charges are regularly grouped behind the traveling laser pulse; c) plasma wave follows the laser pulse, accelerating trapped electrons

Fig.13 Laser-driven plasma accelerators: a) laser wakefield accelerator (LWFA), requires short laser pulse $\tau_L \approx \lambda_p/2c$; b) laser beat wave accelerator (LBWA), requires two laser beams with $\omega_1 - \omega_2 = \omega_p$; c) self-modulated LWFA, requires relativistically strong laser pulse

Fig.14 Electron acceleration in prefilled plasma channel with an s-polarized laser pulse at a=1, $\omega_p^{ch}/\omega = 0.065$, $\omega t/2\pi$=4000, E_e^0=50 MeV: a) longitudinal phase space of the beam electrons; b) x-y distribution of the beam electrons; c) longitudinal wake electric field: d) profile of the pulse electromagnetic energy[7]

Fig.15 Reflection from plasma gradient at oblique incidence

Fig.16 Channeling by axicon focused laser beams: a) expanding plasma channel by gas breakdown with linear polarized laser beam; b) stationary plasma channel produced by radially polarized laser beam

Fig.17 Plasma channel produced by cylindrical shock wave

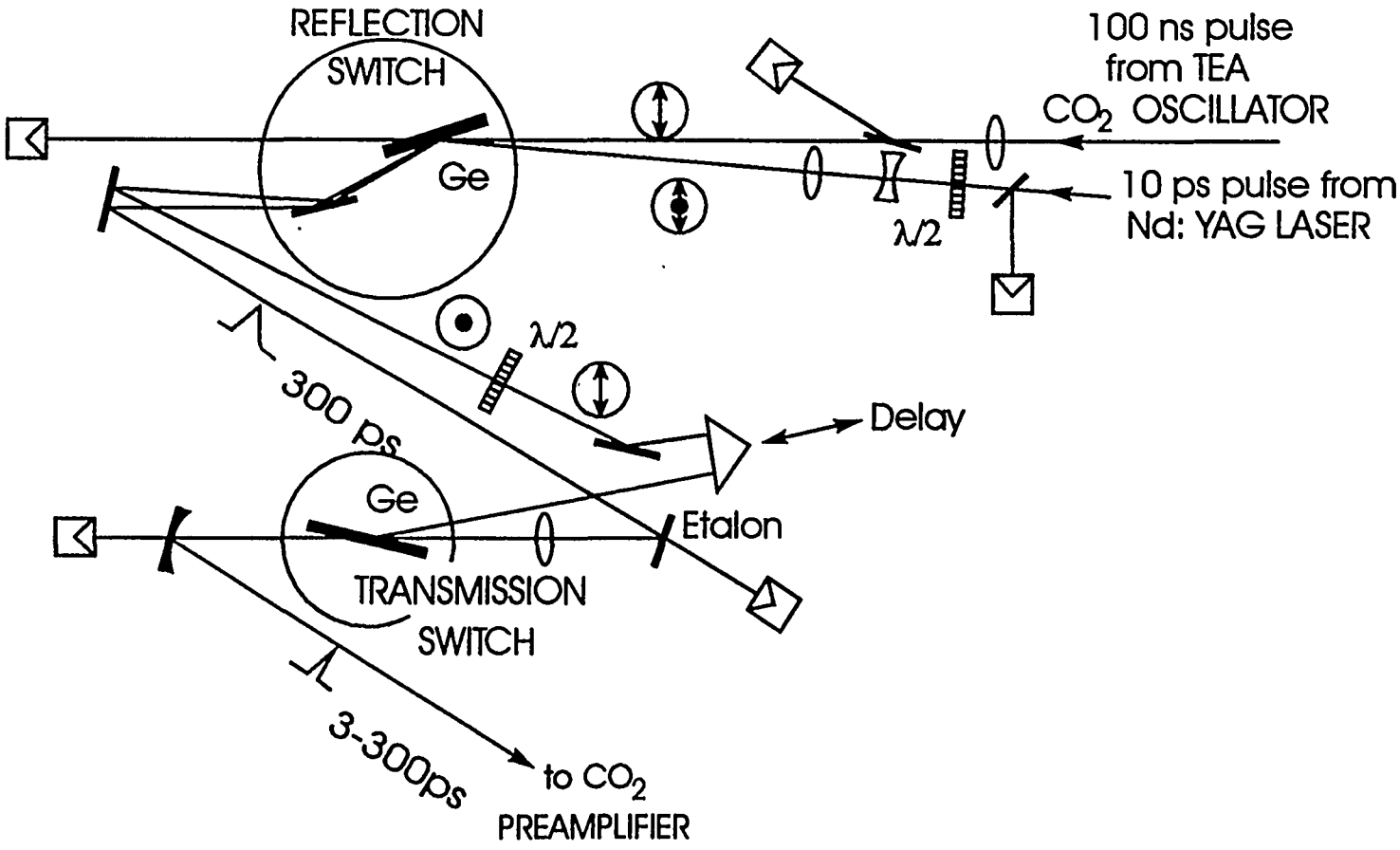

Fig.1 Principle optical diagram of the picosecond slicing set-up

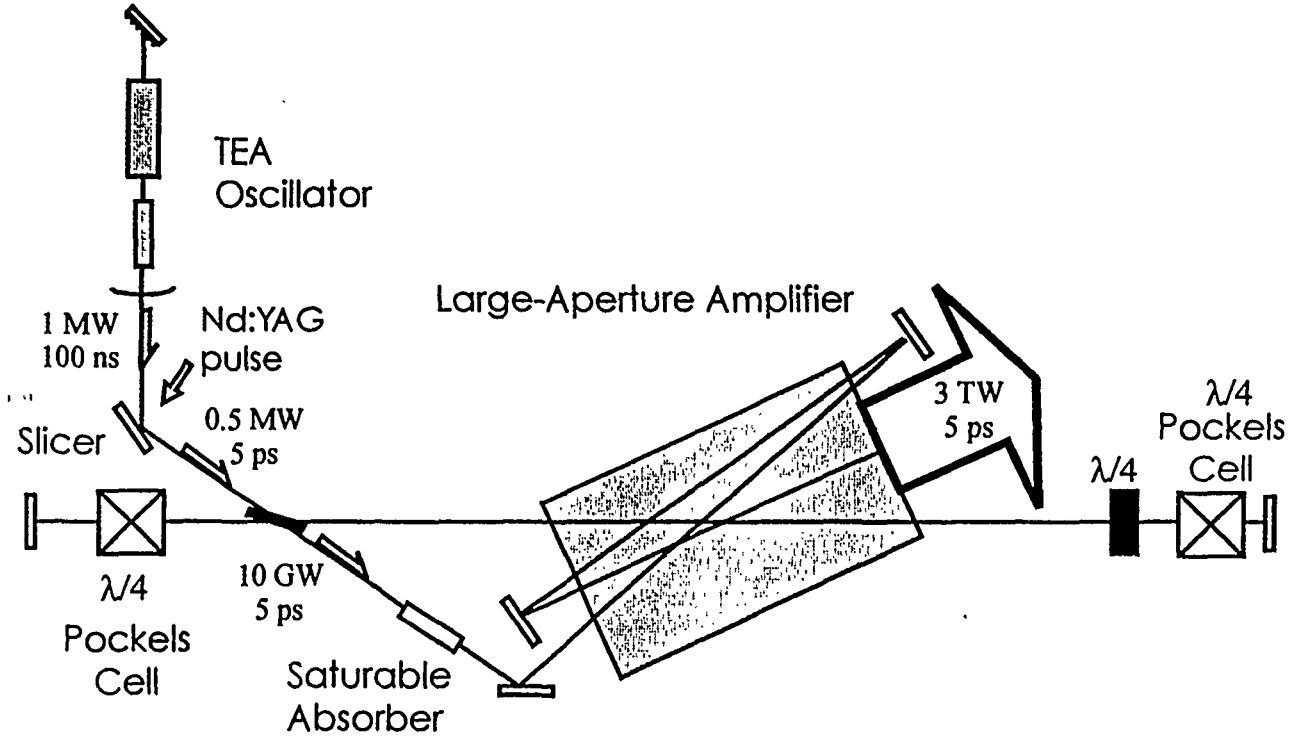

Fig.2 Principle optical diagram of the psTW-CO_2 laser system

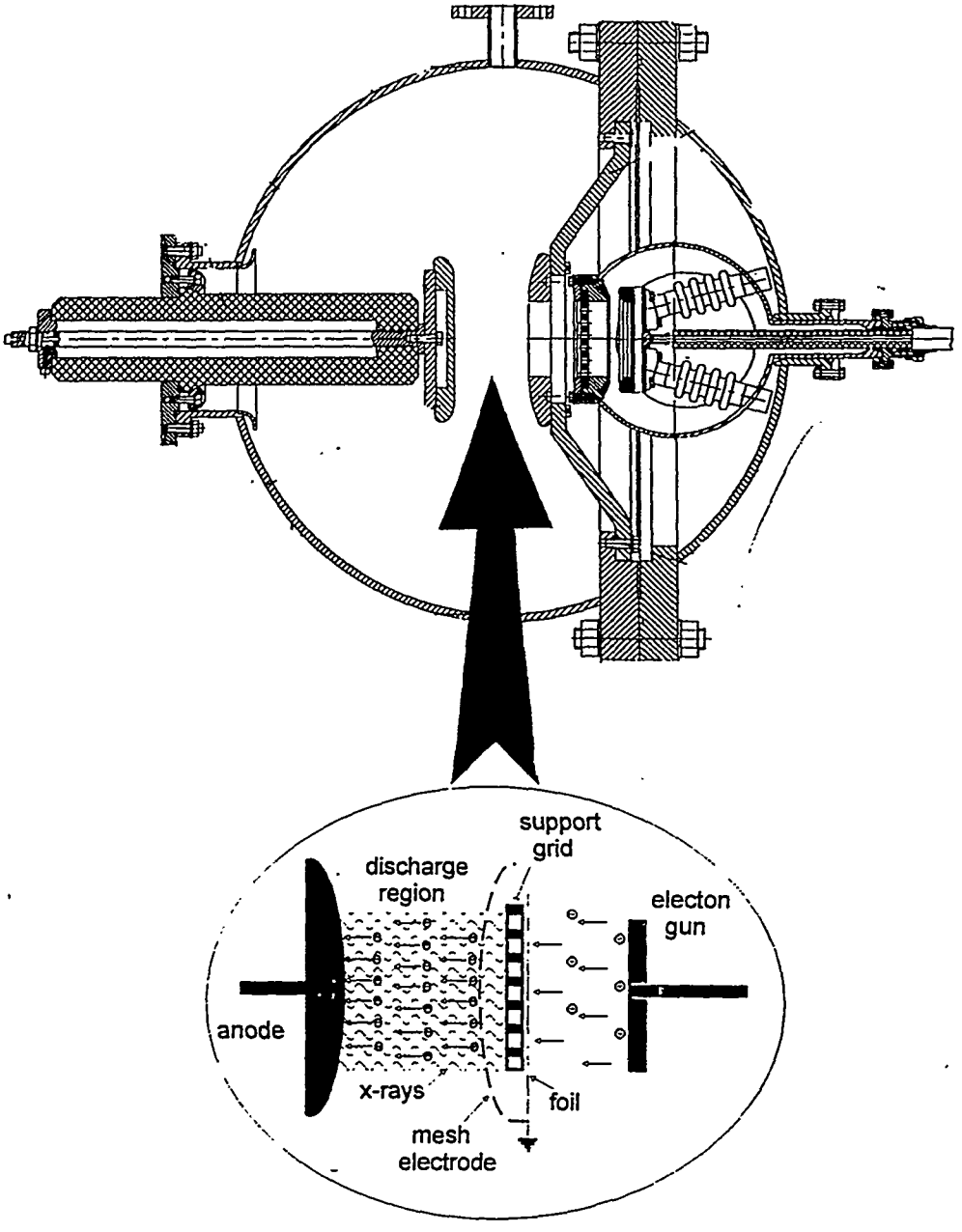

Fig.3 Cross-sectional diagram of the x-ray preionized CO_2 laser amplifier

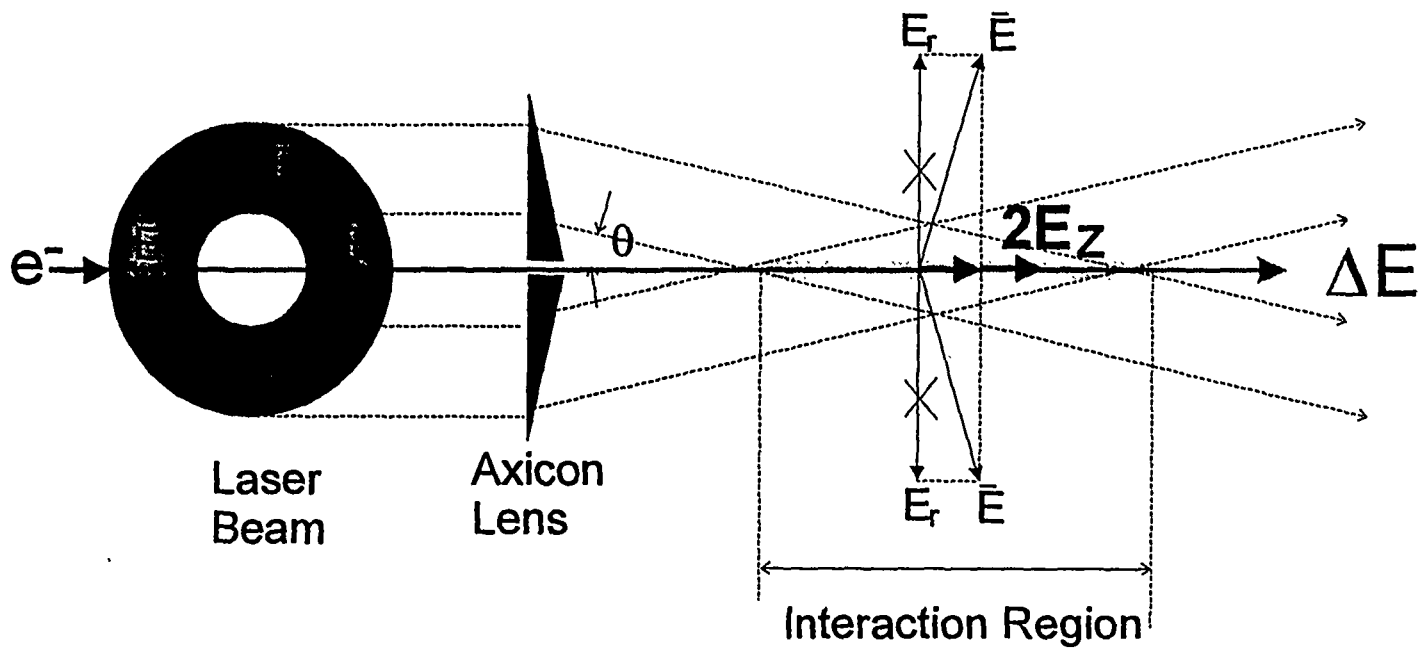

Fig.4 Axicon focusing of radially polarized laser beam in the Inverse Cherenkov Accelerator

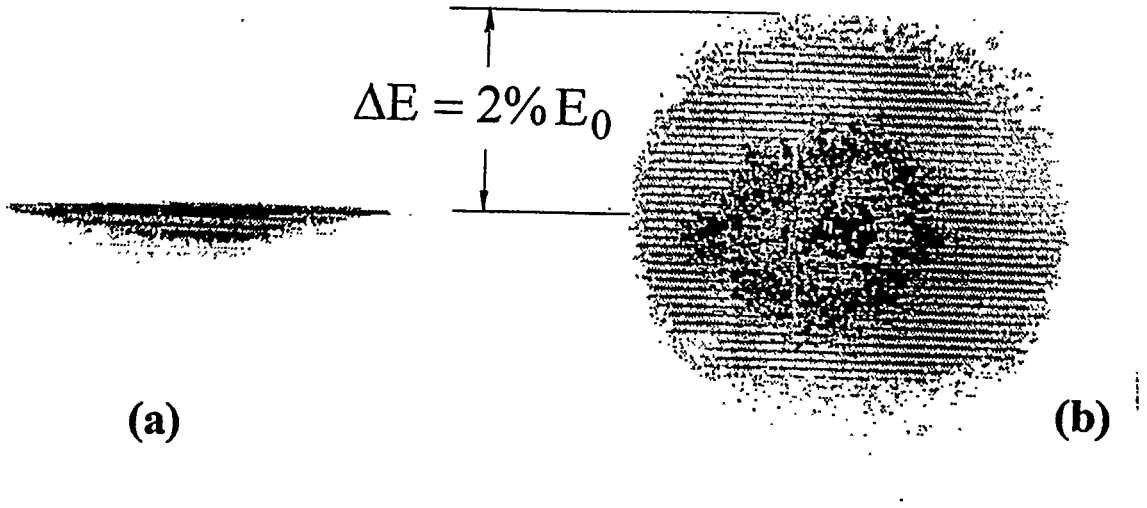

Fig.5 Snap-shots of the electron spectrometer screen without laser (a) and with ~1-GW laser pulse delivered to the ICA cell (b)

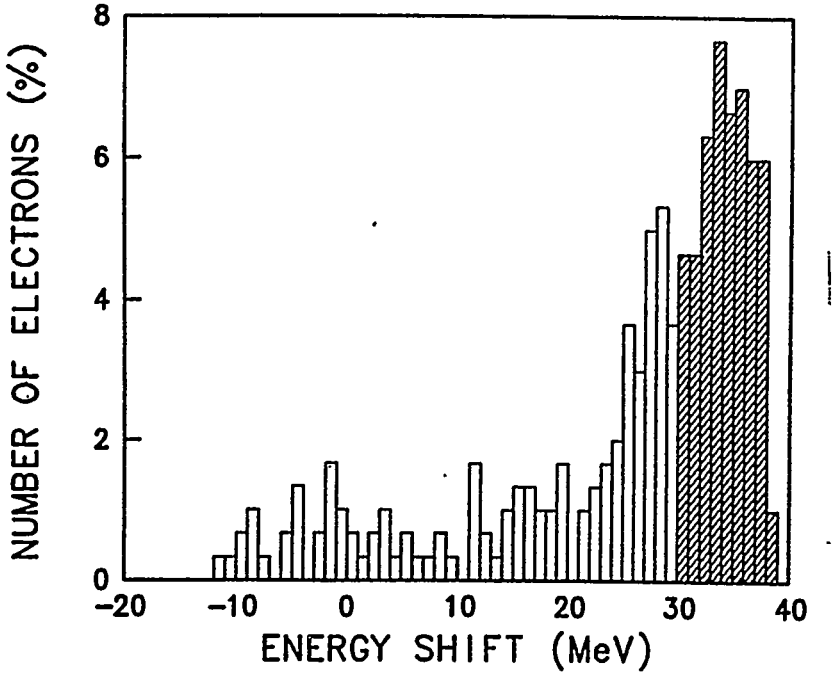

Fig.6 Monte-Carlo computer simulation for Inverse Cherenkov acceleration of prebunched electrons: initial electron energy 50 MeV, CO_2 laser power 50 GW, Cherenkov angle θ=20 mrad, interaction length 20 cm[25]

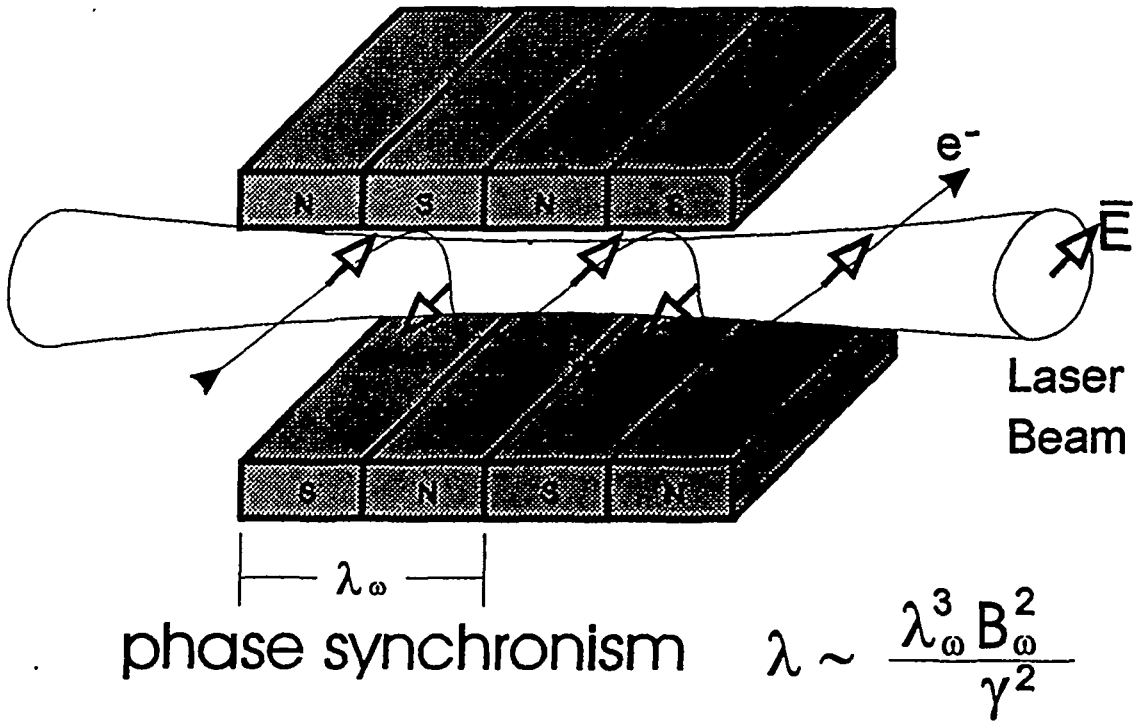

Fig.7 Principle diagram of the IFEL accelerator

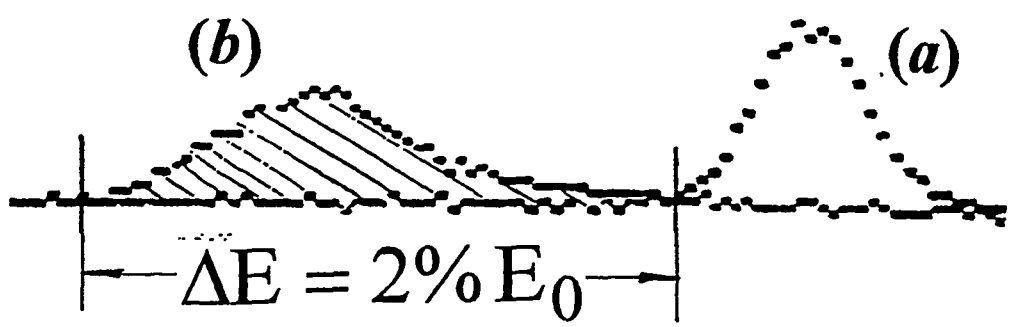

Fig.8 Electron beam distributions obtained on a phosphor screen placed downstream of the dipole bending magnet at the end of the IFEL beamline:(a) no laser; (b) with 0.5 GW laser power; E(linac)=40 MeV, B_w=10 kG, λ_w=2.9-3.1 cm

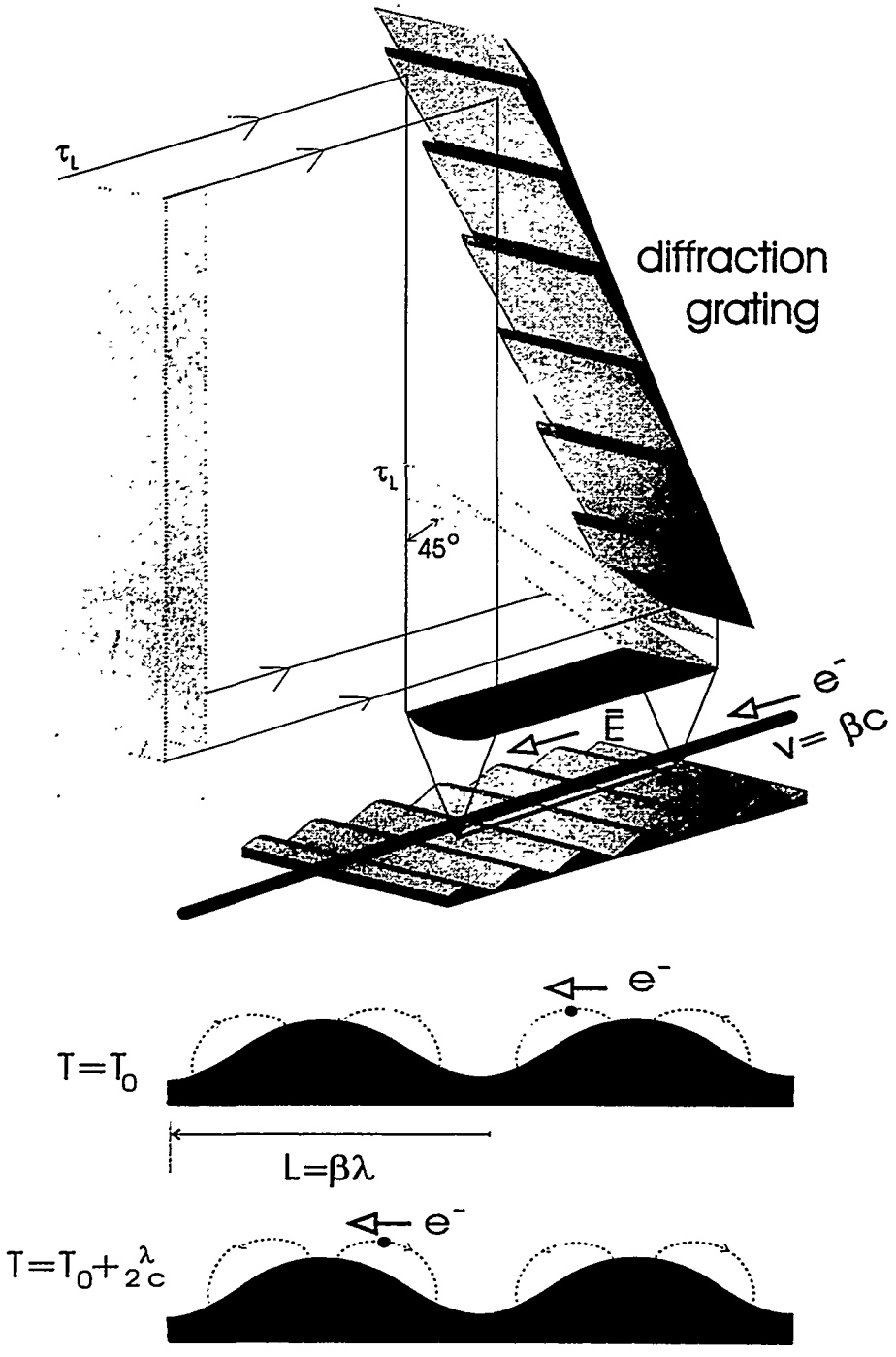

Fig.9 Principle diagram of the grating linac

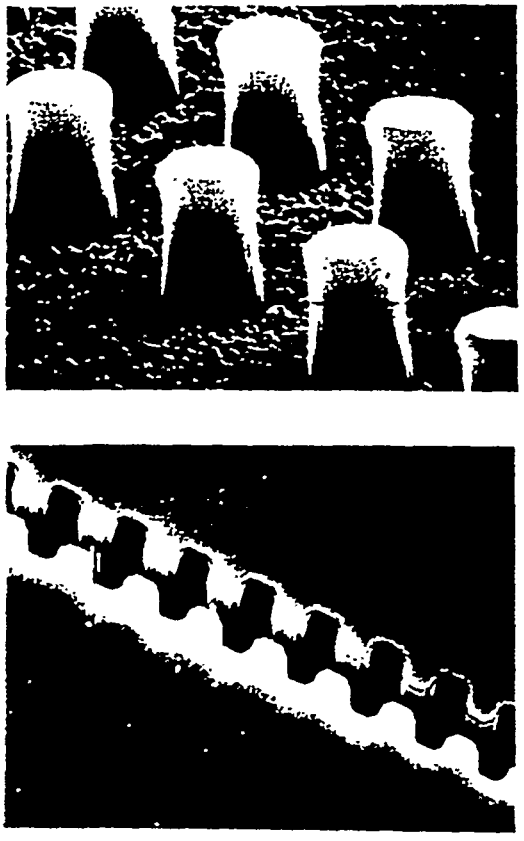

Fig.10 Examples of the 10-μm period structures for the grating linac[22]

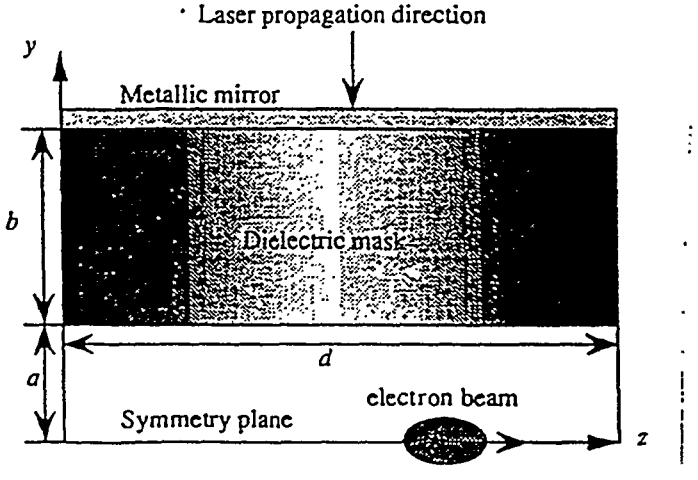

Fig.11 Schematic of the top half of one period of a dielectric loaded laser resonant acceleration structure[13]

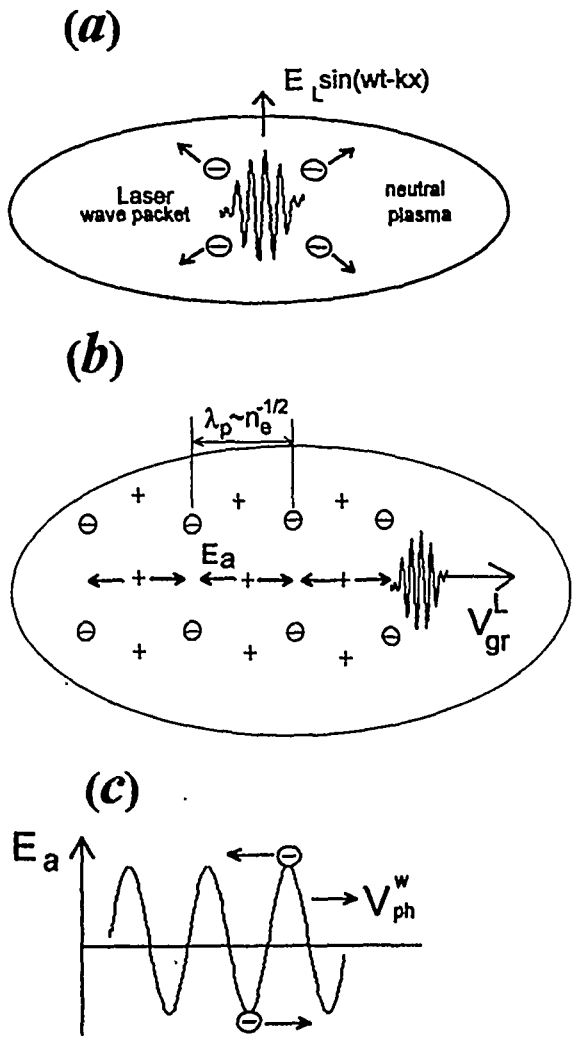

Fig.12 Laser excited plasma wake:a) wave packet ponderomotively separates charges; b) charges are regularly grouped behind the traveling laser pulse; c) plasma wave follows the laser pulse, accelerating trapped electrons

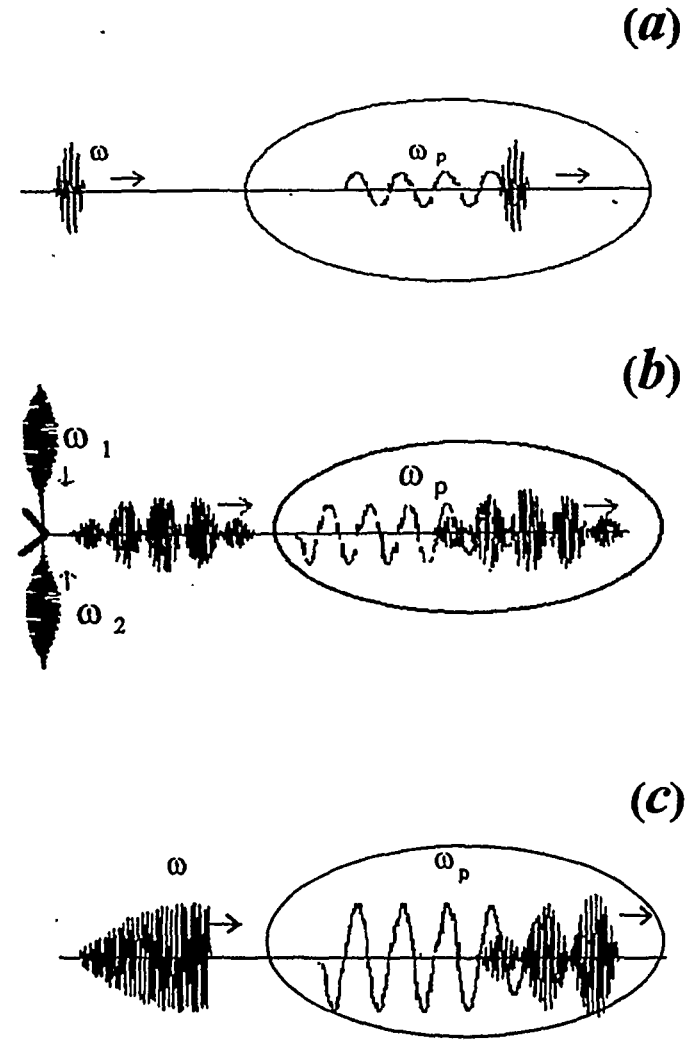

Fig.13 Laser-driven plasma accelerators: a) laser wakefield accelerator (LWFA), requires short laser pulse $\tau_L \approx \lambda_p/2c$; b) laser beat wave accelerator (LBWA), requires two laser beams with $\omega_1 - \omega_2 = \omega_p$; c) self-modulated LWFA, requires relativistically strong laser pulse

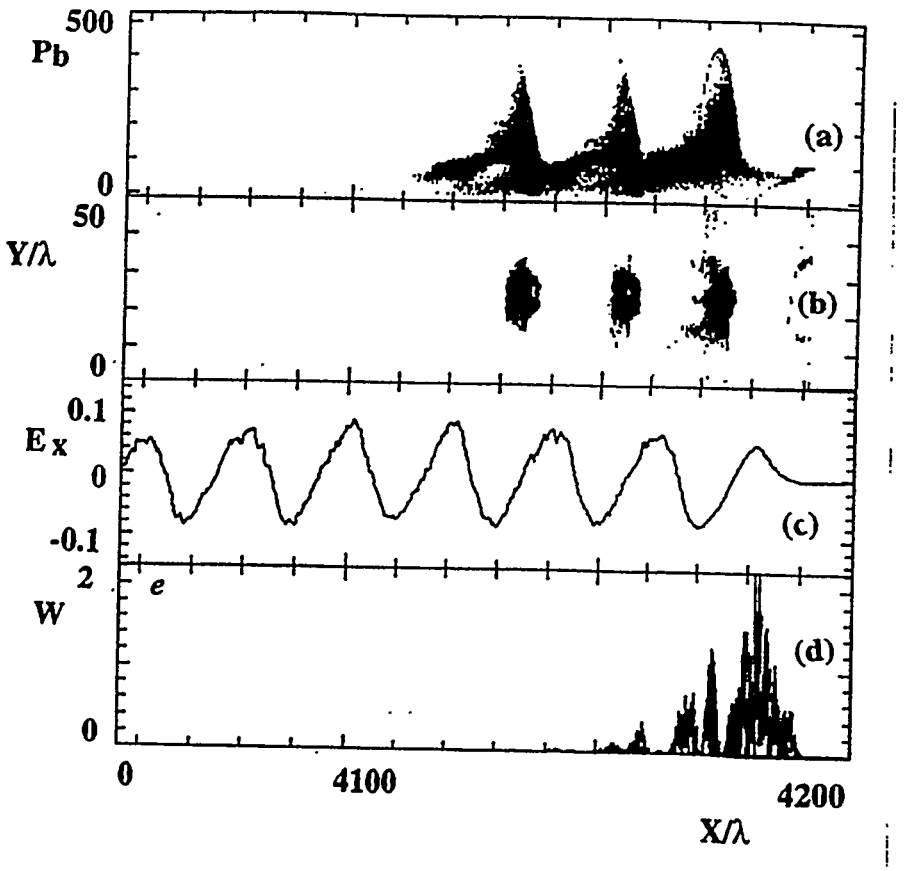

Fig.14 Electron acceleration in prefilled plasma channel with an s-polarized laser pulse at a=1, $\omega_p^{ch}/\omega = 0.065$, $\omega t/2\pi$=4000, E_e^0=50 MeV: a) longitudinal phase space of the beam electrons; b) x-y distribution of the beam electrons; c) longitudinal wake electric field: d) profile of the pulse electromagnetic energy[7]

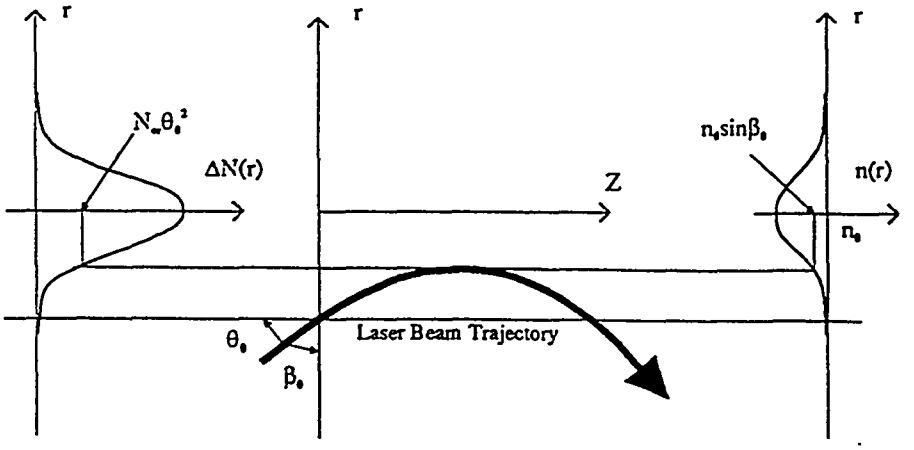

Fig.15 Reflection from plasma gradient at oblique incidence

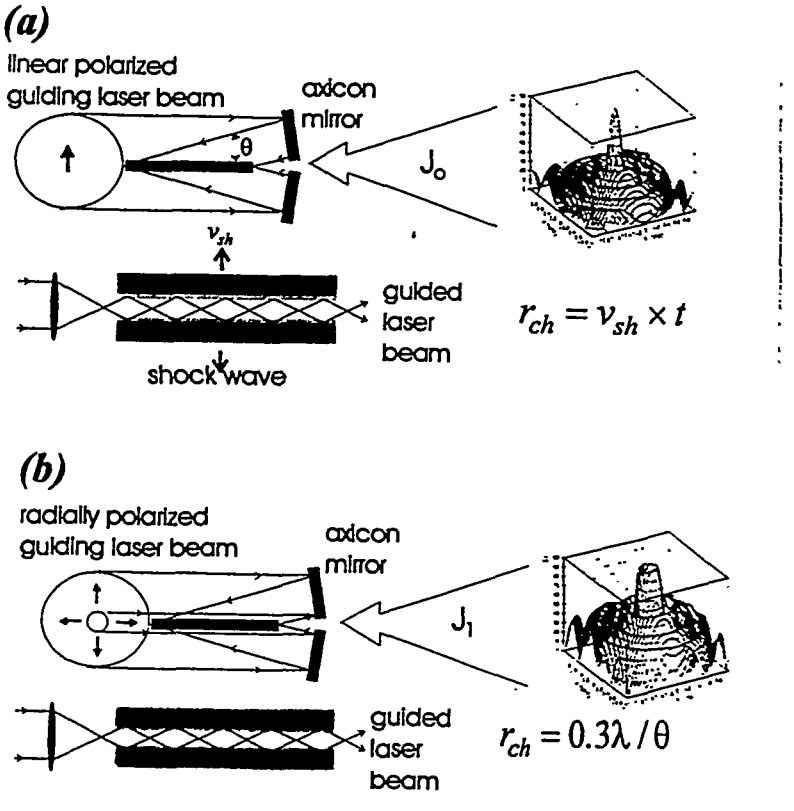

Fig.16 Channeling by axicon focused laser beams: a) expanding plasma channel by gas breakdown with linear polarized laser beam; b) stationary plasma channel produced by radially polarized laser beam

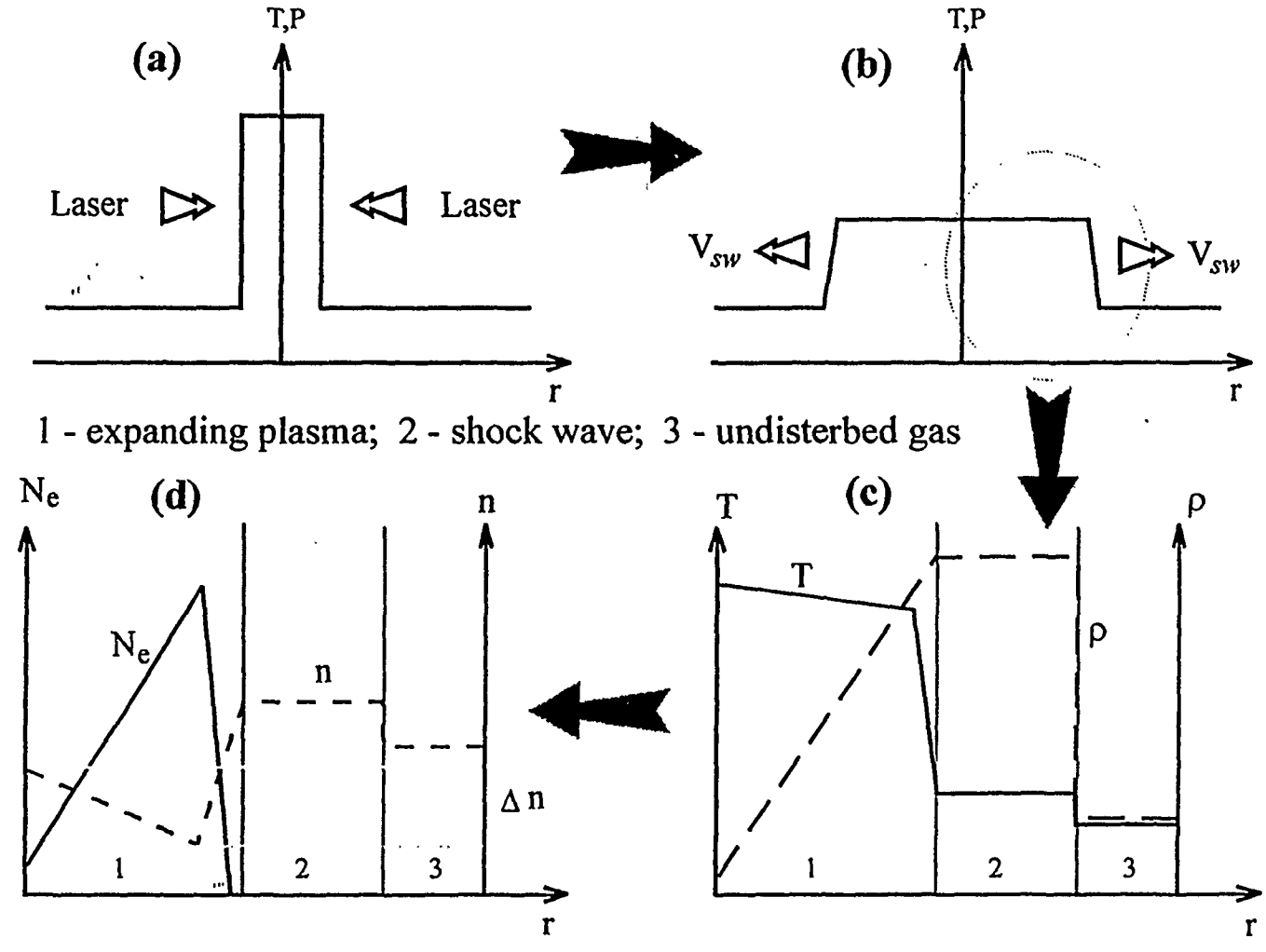

Fig.17 Plasma channel produced by cylindrical shock wave